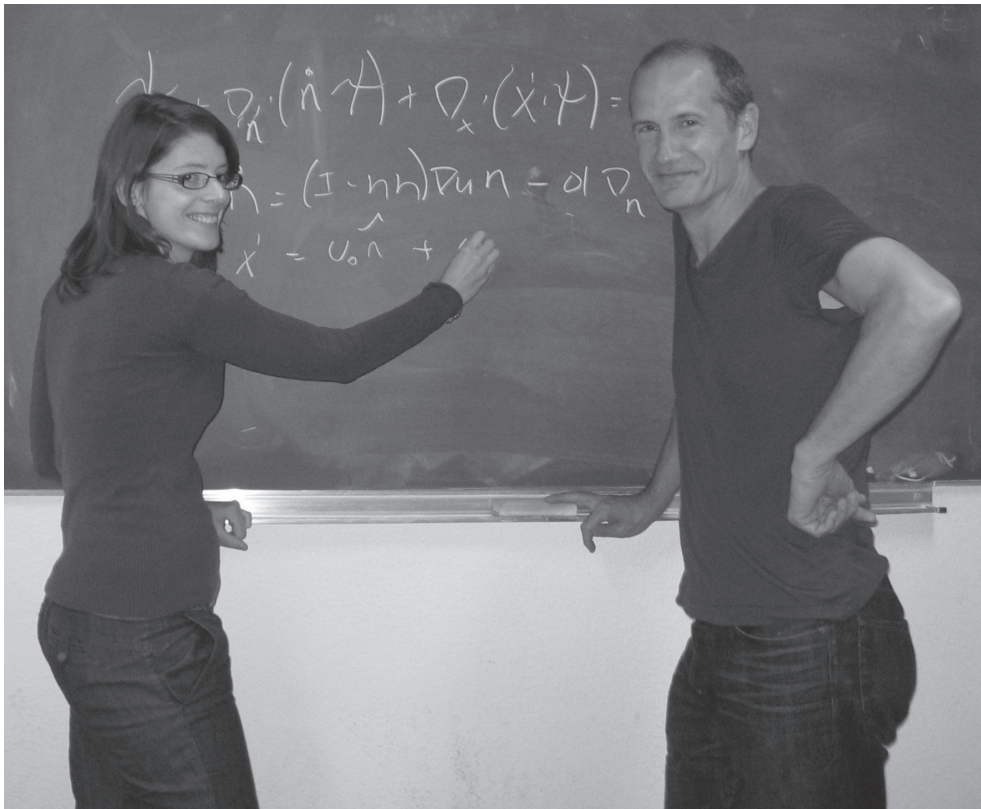# 3
Dynamics of complex biofluids

Christel HOHENEGGER and Michael J. SHELLEY

Courant Institute of Mathematical Sciences, New York University

3.1   Introduction

Complex fluids, such as polymer solutions, particulate suspensions, and many biological fluids, form a broad class of liquids whose mechanical and dynamical properties must be described on multiple length scales. In recent years, biological flow phenomena involving complex fluids, such as peristaltic pumping and sperm motility in the reproductive tracts, have received much attention. It has also been fruitful to consider systems such as bacterial baths as complex fluids themselves when describing them at the macroscopic scale. One of the most challenging issues when characterizing the transport properties of these systems is capturing the interactions between the fluid and the suspended microstructures (e.g. polymer coils, colloidal particles, flexible and rigid fibers, and "active" particles such as bacteria). This is important, as it is these couplings that lead to very complicated dynamical structures and large-scale flow associated with mixing or enhanced swimming efficiency. In many cases, numerical simulations are as challenging as model development, since complex fluid systems can have many degrees of freedom.

The general field of complex fluids presents many interesting flow phenomena and important applications, such as elastic turbulence and low-Reynolds-number mixing (Groisman and Steinberg 2001, 2004), microscopic to macroscopic instabilities such as coil-stretch (Arratia *et al.* 2006; Thomases and Shelley 2009) and stretch-coil (Young and Shelley 2007), and the use of viscoelastic nonlinearities to perform logical operations in microfluidic chips (Groisman and Quake 2004). Of particular interest here are transport phenomena in active suspensions and complex fluids. This includes mixing, pumping, and swimming, both of single organisms and collectively. The most classical problem of swimming, in a biological fluid is that of sperm motility. In studies of collective dynamics, Dombrowski *et al.* (2004) have observed the emergence of large-scale vortices and jets in suspensions of swimming *B. subtilis.* The possible utility of the transport and mixing in these systems has driven the development of artificial analogues, such as the chemically driven synthetic microswimmers fabricated by Paxton *et al.* (2004), which mimic the motile behavior of swimming bacteria.

The general mathematical framework for the derivation of many complex fluid models can be summarized as follows. Consider a small fluid volume moving with the fluid, filled with many "particles", and over which the macroscopic velocity field and its gradient can be assumed uniform. Given the current configuration of the particles, approximate the "extra" stress that these particles induce in the surrounding fluid. The evolution of the particle configuration (location, orientation, distension, etc.), from which one approximates this extra stress, is described by a Smoluchowski equation (or conservation of probability). The inclusion of the extra stress as a source of force in the macroscopic momentum balance equations for a continuous medium often closes the system. In Section 3.2 we develop these ideas, which from the basics of non-Newtonian fluid mechanics. We then focus on the two main examples, of rod-shaped and dumbbell-shaped immersed particles. The latter is a necessary element in the derivation of the Oldroyd-B model and is described in Section 3.3. In order to find the extra stress due to a suspension of rod-like bodies, the Kirkwood formula is recalled in Section 3.2.3 and its application to an actively swimming rod is presented. The last section,

Section 3.4, consists of an overview of recent work on two important applications, pumping and swimming. In-depth details are given about the continuum model describing a suspension of active rods and its stability behavior around a state of uniformity and isotropy.

3.2   Basics of non-Newtonian fluid mechanics

3.2.1   Conservation of probability

We consider a particle whose initial configuration (e.g. orientation, center of mass, length, and volume) is given by $\mathbf{z}$ and which evolves according to

$$\frac{d\mathbf{Z}}{dt} = \mathbf{V}(\mathbf{Z}, t), \qquad \mathbf{Z}(\mathbf{z}, 0) = \mathbf{z}.$$

Example 1 (dumbbell). The configuration variables are the position of the center of mass $\mathbf{X}_c$ and the end-to-end vector $\mathbf{R}$.

Example 2 (rod). The configuration variables are the position of the center of mass $\mathbf{X}_c$ and the orientation vector $\mathbf{p}$, with $|\mathbf{p}| = 1$.

Let $\Psi(\mathbf{Z}, t)$ be the probability density for realizing a set of configuration variables $\mathbf{Z}$ at time t, and let $\Omega(t) \subset \mathbb{R}^n$ be an arbitrary volume that tracks a set of particle trajectories from the initial configuration $\mathbf{z}$ through configuration space.

The "number" of particles in this evolving set, defined as $N = \int_{\Omega(t)} \Psi(\mathbf{Z}, t)\, dV_Z$, is taken to be conserved. Diffusional processes will be added later. To express N in the Lagrangian frame, we define the flow map $\mathbf{J} = \nabla_z \mathbf{Z}$. The derivation of the conservation of probability follows the same argument as for the conservation of mass in a continuum medium. First, by a change of variable, we express N in the reference configuration $\Omega(0)$. Next, using Liouville's formula $\partial_t \mathbf{J} = (\nabla_Z \cdot \mathbf{V})J$ ($J = \det \mathbf{J}$) and the fact that N is conserved, we have

$$0 = \frac{dN}{dt} = \int_{\Omega(0)} \left[\frac{\partial \Psi}{\partial t} + \mathbf{V} \cdot \nabla_Z \Psi + (\nabla_Z \cdot \mathbf{V})\Psi \right] J \, dV_Z.$$

Transforming back to the arbitrary $\Omega(t)$, we arrive at the Smoluchowski equation,

$$\frac{\partial \Psi}{\partial t} + \nabla_Z \cdot (\mathbf{V}\Psi) = 0. \tag{3.1}$$

In order to close eqn (3.1), we need boundary and initial conditions, as well as equations for the particle fluxes $\mathbf{V}$.

3.2.2   Kinematics of rods and dumbbells

We now develop kinematic equations for immersed rod and dumbbell- shaped particles.

68 *Dynamics of complex biofluids*

3.2.2.1 *Rods*

First, consider a slender object immersed in a Newtonian Stokesian fluid, described by its centerline $\mathbf{X}(s,t)$, with s being its arc length (Batchelor 1970b; Keller and Rubinow 1976; Johnson 1980). Here, we make use of the local slender-body-theory approximation to the centerline velocity $\mathbf{V}(s,t)$,

$$8\pi\mu\left[\mathbf{V}(s,t) - \mathbf{U}(\mathbf{X},t)\right] = -c(\mathbf{I} + \mathbf{X}_s\mathbf{X}_s^{\mathrm{T}})\mathbf{f}, \qquad (3.2)$$

where $c = \ln(e\varepsilon^2) < 0$, with $\varepsilon \ll 1$ being the particle aspect ratio, $\mathbf{U}(\mathbf{X},t)$ is the background velocity field, and $\mathbf{f}$ is the force per unit length exerted by the rod upon the fluid. For brevity, we define $\eta = 8\pi\mu/(-c) > 0$.

We will study three examples in detail: a straight rod in a linear background flow, and a straight rod that locomotes through a prescribed surface stress, considered both in the absence of a background flow and in a linear background flow.

Example 3 (straight rod in a linear background flow). Consider a rigid rod of fixed length l described by its center of mass and orientation: $\mathbf{X}(s,t) = \mathbf{X}_\mathrm{c}(t) + s\mathbf{p}(t)$ for $-l/2 \leq s \leq l/2$ and $|\mathbf{p}| = 1$. The background flow is taken as linear: $\mathbf{U}(\mathbf{X}) = \mathbf{A}\mathbf{X}$, with $\mathrm{tr}(\mathbf{A}) = 0$. We determine $\mathbf{f}$ and the evolution equations for $\mathbf{X}_\mathrm{c}$ and $\mathbf{p}$ under the conditions of zero net force and torque. Integrating eqn (3.2) with respect to s and using the zero-force condition yields

$$\dot{\mathbf{X}}_\mathrm{c} = \mathbf{A}\mathbf{X}_\mathrm{c}, \qquad \mathbf{f} = s\mathbf{f}_1, \qquad (3.3)$$

where $\dot{\mathbf{X}}_\mathrm{c} = \partial\mathbf{X}/\partial t$. From the zero-torque condition it follows that $\mathbf{f}_1 = \alpha\mathbf{p}$. Substituting eqn (3.3) into eqn (3.2) gives $\eta(\dot{\mathbf{p}} - \mathbf{A}\mathbf{p}) = 2\alpha\mathbf{p}$. Since $\mathbf{p}\cdot\dot{\mathbf{p}} = 0$, α is found by taking the dot product of the last equality with $\mathbf{p}$. Combining everything, we obtain Jeffery's equation (Jeffery 1922),

$$\dot{\mathbf{p}} = (\mathbf{I} - \mathbf{p}\mathbf{p}^{\mathrm{T}})\mathbf{A}\mathbf{p}. \qquad (3.4)$$

The force per unit length is therefore $\mathbf{f} = -(\eta s/2)(\mathbf{p}^T\mathbf{A}\mathbf{p})\mathbf{p}$.

Example 4 (propulsive rod with no background flow). Consider a rod where a constant propulsive tangential stress $-f_\parallel\mathbf{p} = -2\pi ag\mathbf{p}$, where a is the particle radius and g is the magnitude of the stress, is imposed on one half of its length (without loss of generality, for $s < 0$) and a no-slip condition is imposed on the other half ($s > 0$) (Saintillan and Shelley 2007). This model is an idealization of a "Pusher", such as *B. subtilis*, which generates a thrust (via rotary flagellar motion) through its trailing flagellar bundle (schematically illustrated in Fig. 3.1). In this case, eqn (3.2) becomes

$$\eta\left[U + u_\parallel(s)\right]\mathbf{p} = (\mathbf{I} + \mathbf{p}\mathbf{p}^{\mathrm{T}})\mathbf{f}_1, \quad -\frac{l}{2} \leq s \leq 0, \qquad (3.5)$$

$$\eta U\mathbf{p} = (\mathbf{I} + \mathbf{p}\mathbf{p}^{\mathrm{T}})\mathbf{f}_2, \quad 0 \leq s \leq \frac{l}{2}, \qquad (3.6)$$

where $\mathbf{f}_1 = -f_\parallel\mathbf{p} = -2\pi ag\mathbf{p}$ is the motive force per unit length exerted by the rod on the fluid, $\dot{\mathbf{X}}_\mathrm{c} = U\mathbf{p}$ is the translational velocity of the rod, $\mathbf{u}_s = u_s(s)\mathbf{p}$ is the
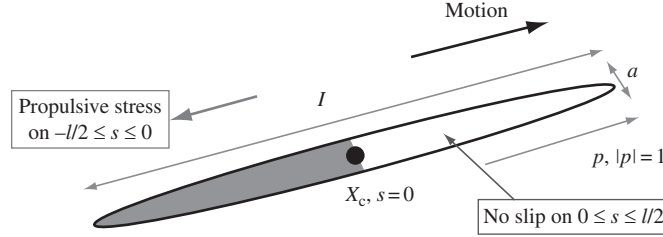
Fig. 3.1   An ellipsoidal rod with propulsive stress on the posterior half of its body.

surface slip velocity, and $\mathbf{f}_2(s) = f_1\mathbf{p}$ is the drag force. The zero-force condition yields $f_2 = f_\parallel$, and thus we have $U = (2/\eta)f_\parallel$ and $u_s = -(4/\eta)f_\parallel$. Using the fact that $\eta = 8\pi\mu/|\ln(e\varepsilon^2)|$, we rewrite U as

$$U = \frac{\varepsilon|\ln(\varepsilon^2 e)|}{2}\frac{lg}{\mu} = \kappa_2\frac{lg}{\mu}, \tag{3.7}$$

where $\kappa_2 = \varepsilon|\ln(\varepsilon^2 e)|/2$ is a purely geometric constant. We will use this expression later as the individual swimming speed in a suspension of many rods.

Example 5 (propulsive rod in linear background flow). We now look at the same rod model swimming within a linear background flow $\mathbf{U} = \mathbf{AX}$. Equation (3.2) becomes

$$\eta\left[\dot{\mathbf{X}}_c + \mathbf{u}_s\mathbf{p} + s\dot{\mathbf{p}} - \mathbf{A}(\mathbf{X}_c + s\mathbf{p})\right] = (\mathbf{I} + \mathbf{pp}^\mathrm{T})\mathbf{f}_1(s), \quad -\frac{l}{2} \le s \le 0, \tag{3.8}$$

$$\eta\left[\dot{\mathbf{X}}_c + s\dot{\mathbf{p}} - \mathbf{A}(\mathbf{X}_c + s\mathbf{p})\right] = (\mathbf{I} + \mathbf{pp}^\mathrm{T})\mathbf{f}_2(s), \quad 0 \le s \le \frac{l}{2}. \tag{3.9}$$

From the zero-torque condition, both $\mathbf{f}_1$ and $\mathbf{f}_2$ are in the $\mathbf{p}$-direction. Therefore, we set $\mathbf{f}_1 = -f_\parallel(s)\mathbf{p} = -(f_0 + f_1 s)\mathbf{p}$ and $\mathbf{f}_2 = (f_2 + f_3 s)\mathbf{p}$. As in Example 4, we consider only a constant propulsive force $f_0 = 2\pi ag$ and thus a slip velocity $u_s(s)$ independent of s. Upon integration of eqns (3.8) and (3.9) with respect to arc length, we obtain the kinematic equation of the center of mass,

$$\dot{\mathbf{X}}_c = \mathbf{AX}_c - \frac{u_s}{2}\mathbf{p}. \tag{3.10}$$

Substituting into eqns (3.8) and (3.9), taking the dot product with $\mathbf{p}$, and comparing coefficients in s allows us to find all the remaining unknowns: $u_s = -4/\eta f_0$, $f_2 = f_0$, $f_1 = (\eta/2)\,\mathbf{p}^\mathrm{T}\mathbf{Ap}$, and $f_3 = -(\eta/2)\,\mathbf{p}^\mathrm{T}\mathbf{Ap}$. From these expressions, we obtain again Jeffery's equation (3.4), and $\dot{\mathbf{X}}_c = \mathbf{AX} + (2/\eta)\,f_0\mathbf{p}$.

Summarizing the kinematic equations for a general disturbance flow whose rate-of-strain tensor is constant, we denote by $\mathbf{u}$ the linearized velocity field around the body and denote its gradient by $\nabla_x\mathbf{u}$. Again, we impose a constant propulsive stress $f_\parallel = f_0 = 2\pi ag$ on the posterior half of the body, and we let $U = \kappa_2 lg/\mu$ be the swimming speed of an individual rod of length l. We have

70   *Dynamics of complex biofluids*

$$\dot{\mathbf{X}}_c = \mathbf{u} + U\mathbf{p} - d_x \nabla_x \ln \Psi, \tag{3.11}$$

$$\dot{\mathbf{p}} = (\mathbf{I} - \mathbf{p}\mathbf{p}^{\mathrm{T}})\nabla_x \mathbf{u}\mathbf{p} - d_p \nabla_p \ln \Psi, \tag{3.12}$$

where we have introduced translational and rotational diffusion processes with phase space (not particle) diffusion coefficients d_x and d_p, respectively (Doi and Edwards 1986). Equations 3.11 and 3.12 give the particle fluxes of the Smoluchowski equation.

3.2.2.2   *Dumbbells*

We now consider a dumbbell, or bead–spring, model. This model arises when a long polymer chain is modeled as a succession of beads and springs as in Fig. 3.2. The change in conformation of the chain is represented by its end-to-end displacement vector $\mathbf{R}$, and its response to distension is represented through the entropic spring force

$$\mathbf{F}_s = 2k_B T \beta^2 \mathbf{R}, \qquad \beta^2 = \frac{3}{2Nb^2}, \tag{3.13}$$

where k_B is the Boltzmann constant, T is the temperature, N is the number of links, and b is the length of a link (Doi and Edwards 1986; Larson 1995). Henceforth, the end-to-end vector will be considered as that of a simple dumbbell. Assuming that the beads are spherical and neglecting hydrodynamic effects between them, the drag force is $\mathbf{F}^d = (1/2)\,\zeta\left(\dot{\mathbf{R}} - \nabla\mathbf{u}\,\mathbf{R}\right)$, where $\zeta = 6\pi\mu a$ is the Stokes drag and $\nabla\mathbf{u}\,\mathbf{R}$ is the rate of stretching of a fluid element containing the beads. The Brownian force is given by $\mathbf{F}^B = k_B T \nabla_{\mathbf{R}} \ln \Psi$. The balance of forces on the dumbbell gives $\dot{\mathbf{R}}$:

$$\dot{\mathbf{R}} = \nabla\mathbf{u}\,\mathbf{R} - \frac{2k_B T}{\zeta}\left[2\beta^2\mathbf{R} + \nabla_{\mathbf{R}} \ln \Psi\right]. \tag{3.14}$$

Equation (3.11) and eqn (3.12) or (3.14) define the particle fluxes in the Smoluchowski equation (3.1). However, this requires knowledge of $\mathbf{u}$ (and hence $\nabla_x \mathbf{u}$), which
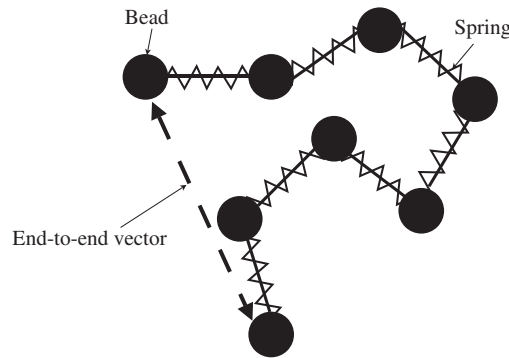

Fig. 3.2   Polymer chain modeled with beads and springs.

is obtained by including both the particle stress produced by the suspension and the Newtonian solvent stress in the macroscopic momentum balance equation:

$$\rho \frac{D\mathbf{u}}{Dt} - \mu \, \Delta_x \mathbf{u} + \nabla_x q = \nabla_x \cdot \boldsymbol{\sigma}^{(p)}, \tag{3.15}$$

where q is the pressure, μ is the Newtonian solvent viscosity, and ρ is the density. Incompressibility is usually assumed, i.e. $\nabla_x \cdot \mathbf{u} = 0$. The extra stress $\boldsymbol{\sigma}^{(p)}$ is given by the Kirkwood formula, which is the subject of the next section.

3.2.3   Kirkwood formula

The Kirkwood formula provides a means for determining the additional or "extra" stress created by particles (rods as dumbbells) suspended in a Newtonian solvent. Details can be found in Doi and Edwards (1986), Larson (1995), and Bird *et al.* (1987).

Example 6 (dumbbells). One basic construction of the Kirkwood formula assumes that the suspension is composed of pairs of beads, with a connecting vector $\mathbf{R}_m$, between which there is a "nonhydrodynamic" force $\mathbf{F}_m$. In particular, given a control volume V, the Kirkwood formula for a suspension of N bead pairs is

$$\boldsymbol{\sigma}^{(p)} = -\frac{1}{V} \sum_{m=1}^{N} \langle \mathbf{F}_m \mathbf{R}_m^{\mathrm{T}} \rangle. \tag{3.16}$$

As in statistical physics, for large N it is useful to replace the average $(1/N) \sum_{n=1}^{N} f_n$ by $\langle f \rangle$, the distributional average of f with respect to the probability density function Ψ.

Therefore, by defining the particle density as $n = N/V$, eqn (3.16) becomes

$$\boldsymbol{\sigma}^{(p)} = -n \langle \mathbf{F} \mathbf{R}^{\mathrm{T}} \rangle. \tag{3.17}$$

The Kirkwood formula as given by eqn (3.17) is particularly suitable for the dumbbell model. Application of eqn (3.17) to the dumbbell model, where $\mathbf{F}$ is the entropic spring force given by eqn (3.13), gives

$$\boldsymbol{\sigma}^{(p)} = 2n k_{\mathrm{B}} T \beta^2 \langle \mathbf{R} \mathbf{R}^{\mathrm{T}} \rangle. \tag{3.18}$$

Example 7 (rods). Another form of the extra stress in a suspension, with slender bodies in mind, was proposed by Batchelor (1970*a*, 1977). Let $\boldsymbol{\sigma}$ be the microscopic stress evaluated on the surfaces ∂B_m of N bodies. Then in a volume V, Batchelor's formula is

$$\boldsymbol{\sigma}^{(p)} = \frac{1}{V} \sum_{m=1}^{N} \int_{\partial B_m} dA \, [\boldsymbol{\sigma} \hat{\mathbf{n}} \mathbf{X}_{\mathrm{c}}^{\mathrm{T}} - \mu(\mathbf{u}\hat{\mathbf{n}}^{\mathrm{T}} + \hat{\mathbf{n}}\mathbf{u}^{\mathrm{T}})]. \tag{3.19}$$

Here $\hat{\mathbf{n}}$ is the unit outward normal to the surface and $\mathbf{u}$ is the microscopic velocity on the surface. For slender bodies, the surface velocity is only a function of the arc length along the centerline, and therefore the surface integral containing $\mathbf{u} = \mathbf{u}(s)$ vanishes.

72   *Dynamics of complex biofluids*

Denoting by $\mathbf{f} = -\boldsymbol{\sigma}\hat{\mathbf{n}}$ the force the body exerts on the fluid, eqn (3.19) therefore reduces to

$$\boldsymbol{\sigma}^{(p)} = -\frac{1}{V} \sum_{p=1}^{N} \int ds\, \mathbf{f}\mathbf{X}^{\mathrm{T}}. \tag{3.20}$$

The Kirkwood formula given by eqn (3.20) leads to the calculation of the extra stress generated by a single rod and then by a suspension of such rods.

Applying eqn (3.20) to a propulsive rod as described in Example 4 gives the contribution to the stress from a single swimmer stress,

$$\mathbf{S} = -\kappa_1 l^3 g\mathbf{p}\mathbf{p}^{\mathrm{T}} = -\sigma_0\mathbf{p}\mathbf{p}^{\mathrm{T}}, \tag{3.21}$$

where $\kappa_1 = (\pi\varepsilon)/2$ is another geometric constant. We remark that the units of $\sigma_0 = \kappa_1 l^3 g$ are force times length; note these are the units of the strength of a force dipole or stresslet.

Next, we combine eqns (3.20) and (3.21) to find the volume-averaged extra stress in a box of volume L^3 containing N such swimmers. We assume that there are M swimmers in a smaller control volume L_M^3 and that the rate-of-strain tensor is constant over this smaller volume. Further, we assume a separation of scales $l \leq L_M \leq L$. After some manipulation, we find

$$\boldsymbol{\sigma}^{(p)} = -nC\sigma_0 \frac{1}{M} \sum_{m=1}^{M} \mathbf{p}\mathbf{p}^{\mathrm{T}}, \tag{3.22}$$

where $n = N/L^3$ is the number density and $C = (M/L_M^3)/(N/L^3)$ is the local concentration.

For large M, the weighted sum converges to the configurational average with respect to Ψ_M, the probability density function for finding a rod with a given center-of-mass position and orientation in the small volume. In passing from the local distribution function and concentration to the macroscopic distribution function, we write $\Psi_M = \Psi/C$ and the extra stress becomes $\boldsymbol{\sigma}^{(p)} = -n\sigma_0\langle\mathbf{p}\mathbf{p}^{\mathrm{T}}\rangle$. Redefining Ψ as $n\Psi$, we obtain the extra stress generated by a suspension of rear-activated swimmers,

$$\boldsymbol{\sigma}^{(p)} = -\sigma_0\langle\mathbf{p}\mathbf{p}^{\mathrm{T}}\rangle. \tag{3.23}$$

As an aside, we note that the normalization of Ψ is $\int dV_x \int dS_p\, \Psi = nL^3$.

3.3   Viscoelastic fluid

One of the simplest models of a viscoelastic fluid is given by the Oldroyd-B equations. There, the polymer chains are modeled as dumbbells (see Fig. 3.2) that have a linear force response to distension. The Smoluchowski equation, eqn (3.1), gives the evolution of a probability density function whose configuration variables are the end-to-end displacement vector $\mathbf{R}$ and the center-of-mass location $\mathbf{X}_c$:

$$\Psi_t + \nabla_{\mathbf{x}} \cdot (\dot{\mathbf{X}}_c \Psi) + \nabla_{\mathbf{R}} \cdot (\dot{\mathbf{R}}\Psi) = 0. \tag{3.24}$$

Again, the Oldroyd-B model assumes that the force exerted by the dumbbell is that of a linear spring given by eqn (3.13). The particle fluxes are given by $\dot{\mathbf{X}}_c = \mathbf{u}$ and eqn (3.14) for $\dot{\mathbf{R}}$ (here, the effect of center-of-mass diffusion has been neglected). The macroscopic velocity $\mathbf{u}$ satisfies the momentum conservation equation (3.15), which balances viscous stress against the extra stress given by the Kirkwood formula, eqn (3.18).

Because of the simple Hookean response in the Oldroyd-B model, a macroscopic evolution equation for $\boldsymbol{\sigma}^{(p)}$ can be found directly, without recourse to any "closure approximation". Substituting the expressions for the particle fluxes into eqn (3.24) together with incompressibility yields

$$\Psi_t + \mathbf{u} \cdot \nabla_x \Psi + \nabla_{\mathbf{R}} \cdot \left[\Psi \nabla_x \mathbf{u}\, \mathbf{R} - \frac{2k_{\mathrm{B}}T}{\zeta} \left(2\beta^2 \mathbf{R}\Psi + \nabla_{\mathbf{R}}\Psi \right) \right] = 0. \tag{3.25}$$

Since $\boldsymbol{\sigma}^{(p)}$ is proportional to $\langle \mathbf{R}\mathbf{R}^{\mathrm{T}} \rangle$, the evolution equation for $\boldsymbol{\sigma}^{(p)}$ is found by multiplying eqn (3.25) by $\mathbf{R}\mathbf{R}^{\mathrm{T}}$ and integrating over the $\mathbf{R}$ volume. The derivation requires the following tensor equalities (Larson 1995):

$$\int dV_{\mathbf{R}}\, \mathbf{R}\mathbf{R}^{\mathrm{T}} \Psi_t = \frac{\partial}{\partial t} \langle \mathbf{R}\mathbf{R}^{\mathrm{T}} \rangle,$$

$$\int dV_{\mathbf{R}}\, \mathbf{R}\mathbf{R}^{\mathrm{T}} \nabla_{\mathbf{R}} \cdot (\Psi \nabla\mathbf{u}\,\mathbf{R}) = - \left[\nabla\mathbf{u}\langle \mathbf{R}\mathbf{R}^{\mathrm{T}} \rangle + \langle \mathbf{R}\mathbf{R}^{\mathrm{T}} \rangle \nabla\mathbf{u}^{\mathrm{T}} \right],$$

$$\int dV_{\mathbf{R}}\, \mathbf{R}\mathbf{R}^{\mathrm{T}} \nabla_{\mathbf{R}} \cdot (\Psi \mathbf{R}) = -2\langle \mathbf{R}\mathbf{R}^{\mathrm{T}} \rangle,$$

$$\int dV_{\mathbf{R}}\, \mathbf{R}\mathbf{R}^{\mathrm{T}} \nabla_{\mathbf{R}} \cdot (\nabla_{\mathbf{R}}\Psi) = 2\mathbf{I}.$$

Applying these identities, we find

$$\frac{D}{Dt}\boldsymbol{\sigma}^{(p)} - \left(\nabla_x \mathbf{u}\, \boldsymbol{\sigma}^{(p)} + \boldsymbol{\sigma}^{(p)} \nabla_x \mathbf{u}^{\mathrm{T}} \right) + \tau^{-1}(\boldsymbol{\sigma}^{(p)} - G\mathbf{I}) = 0, \tag{3.26}$$

where $D/Dt = \partial/\partial t + \mathbf{u} \cdot \nabla$ is the material derivative, $\tau = \zeta/(8k_{\mathrm{B}}T\beta^2)$, and $G = \nu k_{\mathrm{B}}T$. Defining the upper convective derivative $\overset{\triangledown}{\boldsymbol{\sigma}} = D/Dt\boldsymbol{\sigma} - (\nabla_x \mathbf{u}\, \boldsymbol{\sigma} + \boldsymbol{\sigma} \nabla_x \mathbf{u}^{\mathrm{T}})$, eqn (3.26) takes the form

$$\tau \overset{\triangledown}{\boldsymbol{\sigma}}{}^{(p)} + (\boldsymbol{\sigma}^{(p)} - G\mathbf{I}) = 0. \tag{3.27}$$

In a state of rest with no flow, the extra-stress tensor is isotropic: $\boldsymbol{\sigma}^{(p)} = G\mathbf{I}$. Equation (3.27) is called the upper convected Maxwell equation or the Oldroyd-B equation, and is a simple model for a so-called Boger fluid.

Phenomenologically, viscoelastic fluids are characterized by a relaxation time for stress fluctuations. In the Oldroyd-B equations, this timescale is provided by τ. To see this, we rewrite eqn (3.27) in the Lagrangian frame. We denote by $\mathbf{X}$ the Lagrangian

74   *Dynamics of complex biofluids*

variable which gives initial data to the Lagrangian flow map $\mathbf{x} = \chi(\mathbf{X}, t)$, where $\mathbf{x}$ is the Eulerian spatial variable. Let $F_{ij}(t) = \partial x_i / \partial X_j$ be the deformation tensor and $\mathbf{C}(t) = \mathbf{F}^{\mathrm{T}}\mathbf{F}$ be the right Cauchy–Green tensor. It is straightforward to show that $\dot{\mathbf{F}} = \nabla_x \mathbf{u}\, \mathbf{F}$. Multiplying eqn (3.26) by $\mathbf{F}^{-1}$ on the left and by $\mathbf{F}^{-\mathrm{T}}$ on the right, we obtain

$$\left(\mathbf{F}^{-1}\boldsymbol{\sigma}^{(p)}\mathbf{F}^{-\mathrm{T}}\right)_t + \frac{1}{\tau}\left(\mathbf{F}^{(-1)}\boldsymbol{\sigma}^{(p)}\mathbf{F}^{-\mathrm{T}}\right) = \frac{G}{\tau}\mathbf{C}^{-1}. \tag{3.28}$$

Integrating with respect to time then gives

$$\boldsymbol{\sigma}^{(p)}(t) = e^{-t/\tau}\mathbf{F}\boldsymbol{\sigma}^{(p)}(0)\mathbf{F}^{\mathrm{T}} + \frac{G}{\tau}\int_0^t ds\, e^{-(t-s)/\tau}\mathbf{F}(t)\mathbf{C}^{-1}(s)\mathbf{F}^{\mathrm{T}}(t), \tag{3.29}$$

where $\mathbf{F}(0) = \mathbf{I}$. Equation (3.29) shows that memory of the current stress state is lost on a timescale of $O(\tau)$.

To nondimensionalize the Oldroyd-B equation, eqn (3.27), let τ_{f} be some timescale characterizing the fluid flow; for example, given a system length scale L and an external force of size F, this gives $\tau_{\mathrm{f}} = \mu/(\rho L F)$, and we can define the dimensionless relaxation time, the Deborah number, as $De = \tau/\tau_{\mathrm{f}}$. For a shear flow with characteristic time $\dot{\gamma}^{-1} = L/U$ (where L is the channel height and U is the velocity), the Deborah number is replaced by the Weissenberg number $Wi = \tau\dot{\gamma}$.

Rescaling time by τ_{f}, length by L, extra stress by G, and velocity by L/τ_{f}, eqn (3.15) becomes

$$Re\frac{D\mathbf{u}}{Dt} = -\nabla_x p + \triangle_x \mathbf{u} + \beta\nabla_x \cdot \boldsymbol{\sigma}^{(p)},$$

where $\beta = G\tau_{\mathrm{f}}/\mu$ measures the dimensionless size of the extra-stress-to-overall-momentum balance, and $Re = \rho U L/\mu$ is the Reynolds number. Equation (3.27) becomes

$$De\, \overset{\triangledown}{\boldsymbol{\sigma}}{}^{(p)} = -(\boldsymbol{\sigma}^{(p)} - \mathbf{I}).$$

Note that $De\,\beta = \tau G/\mu_{\mathrm{s}}$ is the ratio of the polymer viscosity to the solvent viscosity, and is a material constant. Moreover, in the limit of large Weissenberg number, the Navier–Stokes/Oldroyd-B equations describe an incompressible neo-Hookean solid.

In the next section (Section 3.4), we discuss applications to pumping and to swimming of small organisms, which is characterized by a low Reynolds number but usually not by a low Weissenberg number. Therefore, we replace the Navier–Stokes equations by the Stokes equations and obtain the Stokes–Oldroyd-B (Stokes-OB) equations

$$-\nabla_x p + \triangle_x \mathbf{u} = -\beta\nabla_x \cdot \boldsymbol{\sigma} - \mathbf{f}, \qquad \nabla_x \cdot \mathbf{u} = 0, \tag{3.30}$$

$$Wi\, \overset{\triangledown}{\boldsymbol{\sigma}} = -(\boldsymbol{\sigma} - \mathbf{I}), \tag{3.31}$$

where $\mathbf{f}$ is some external force. Here we have dropped the subscript (p) and are using a Weissenberg number rather than a Deborah number.

Before moving on to applications, we discuss some properties of eqns (3.30) and (3.31). First, we note that the existence of global solutions is unknown, even for two-dimensional flows. A good measure of the stress fluctuations in the system is the relative strain energy $\mathcal{E} = \frac{1}{2} \int dV_x \, \mathrm{tr}(\boldsymbol{\sigma}^{(p)} - \mathbf{I})$. The first property gives an equation for the time evolution of $\mathcal{E}$, while the other two are more general properties and pertain to the mathematical structure of the Stokes-OB equations.

3.3.1   Properties

1. If $\mathbf{E}$ *is the symmetric rate-of-strain tensor, then*

$$\dot{\mathcal{E}} + Wi^{-1} \, \mathcal{E} = \beta^{-1} \left(\int \mathbf{u} \cdot \mathbf{f} - 2 \int \mathbf{E} : \mathbf{E} \right).$$

Physically, $\int \mathbf{u} \cdot \mathbf{f}$ *is the input power from the background force and* $\int \mathbf{E} : \mathbf{E}$ *is the rate of viscous dissipation.*

2. Equations (3.30) and (3.31) lack scale-dependent dissipation.

3. Unlike the Newtonian Stokes equations, eqns (3.30) and (3.31) are not time-reversible.

Proof

1. By the transport theorem, we have $\dot{\mathcal{E}} = (1/2) \, \mathrm{tr} \int D\boldsymbol{\sigma}/Dt$ and, with $D\boldsymbol{\sigma}/Dt$ given by eqn (3.31),

$$\dot{\mathcal{E}} = \frac{1}{2}\mathrm{tr} \int \left[\nabla_x \mathbf{u}\boldsymbol{\sigma} + \boldsymbol{\sigma}\nabla_x \mathbf{u}^{\mathrm{T}} \right] - Wi^{-1} \, \mathcal{E}.$$

This equation can be further simplified by integrating by parts, assuming either periodic or no-slip boundary conditions, to give

$$\dot{\mathcal{E}} = -\frac{1}{2} \int \left[u_i(\nabla_x \boldsymbol{\sigma})_i + u_i(\nabla_x \boldsymbol{\sigma})_i \right] - Wi^{-1} \, \mathcal{E} = -\int \mathbf{u} \cdot (\nabla_x \boldsymbol{\sigma}) - Wi^{-1} \, \mathcal{E}.$$

Substituting eqn (3.30) for $\boldsymbol{\sigma}$, the claim follows by another integration by parts.

2. To understand dissipation in the Stokes-OB equations, we study the dynamics under a small background force perturbation $\mathbf{f} = \varepsilon\mathbf{g}$. Setting $\boldsymbol{\sigma} = \mathbf{I} + \varepsilon\mathbf{T}$ and $p = \varepsilon q$, eqns (3.30) and (3.31) are easily linearized. The linearized polymer extra-stress equation is

$$Wi \left(\frac{\partial \mathbf{T}}{\partial t} - (\nabla_x \mathbf{v} + \nabla_x \mathbf{v}^{\mathrm{T}}) \right) = -\mathbf{T}. \tag{3.32}$$

Assuming a periodicity of 2π, we transform the linearized equations using a spatial Fourier transform with wave vector $\mathbf{k}$. After manipulation of the Fourier transform of the Stokes equations, we obtain the following equation for the $k-$component of the Fourier transform of $\mathbf{T}$:

$$Wi \, \frac{\partial \mathbf{T}_k}{\partial t} = -\mathbf{T}_k - \beta \, Wi \, \mathbf{Q} \left(\frac{\mathbf{k}}{|\mathbf{k}|} \right) \mathbf{T}_k - i\frac{Wi}{k}\mathbf{P} \left(\frac{\mathbf{k}}{|\mathbf{k}|} \right) \mathbf{g}_k,$$

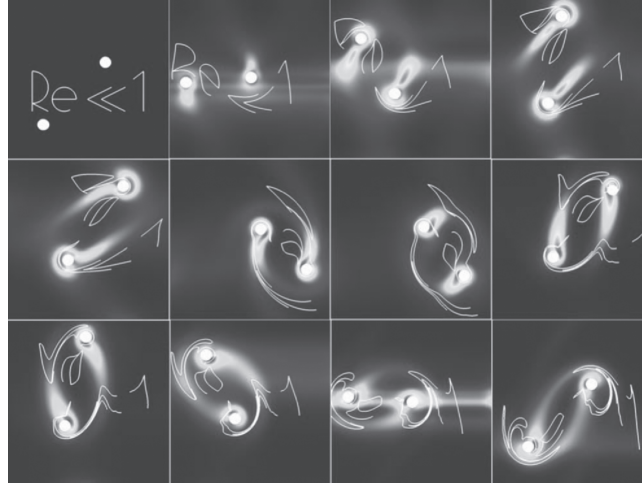**76** *Dynamics of complex biofluids*

Fig. 3.3 Cylindrical pegs used to mix and then unmix a Stokes-OB fluid, showing the time irreversibility of the equations. The gray level represents the normal stress in the fluid. Reproduced with permission from Teran *et al.* (2008).

where **Q** is a rank-four tensor and **P** is a rank-three tensor. Since **Q** depends only upon the direction of the wave vector and not its amplitude, there is no scale-dependent damping.

3. This is immediately apparent from the energy dissipation law of Property 1, and follows by replacing t with $-t$ in eqn (3.31). A striking illustration of this irreversibility is provided by Fig. 3.3, from Teran *et al.* (2008). This figure shows the simulated motion of material points in an Oldroyd-B fluid as a pair of mixing pegs undergo a displacement with time-reversal symmetry (the pegs depart from and arrive back at their initial positions along the same spatio-temporal path). If the dynamics were time reversible, then the labeling "$Re \ll 1$" in the figure, transported as material lines by the flow, would reappear undeformed at the final time. The evolution of the polymer stress is shown by the gray level of the background.

We conclude with two simple rheological flows for the Stokes-OB model that illustrate the model's properties and limitations.

Example 8 (shear flow). We consider a shear flow $\mathbf{u} = (\dot{\gamma}y, 0, 0)$, where $\dot{\gamma}$ is the shear rate between two plates at $z = 0$ and $z = L$, and seek the tensor $\boldsymbol{\sigma}^{(p)}$ in the steady state. From eqn (3.27), we have

$$\boldsymbol{\sigma}^{(p)} = G \begin{pmatrix} 2\,Wi^2 + 1 & Wi & 0 \\ Wi & 1 & 0 \\ 0 & 0 & 1 \end{pmatrix}.$$

The first normal-stress difference is $N_1 = \sigma_{11} - \sigma_{22} = 2G\,Wi^2 > 0$, showing that this system develops normal stresses, as is typically found in viscoelastic fluids. This is unlike the case of a Newtonian fluid, for which $N_1 = 0$. The shear viscosity is likewise calculated as $\mu = \sigma_{12}/\dot{\gamma} = \mu_s + \tau G$, showing that μ is independent of $\dot{\gamma}$, and hence the system does not capture shear thinning. In this sense, the Oldroyd-B equations model a Boger fluid (Larson 1995).

Example 9 (extensional flow). Consider an extensional flow $\mathbf{u} = (\dot{\epsilon}x, -\dot{\epsilon}y/2, -\dot{\epsilon}z/2)$, where $\dot{\epsilon}$ is the elongation rate. The steady-state solution for $\boldsymbol{\sigma}^{(p)}$ is given by

$$\boldsymbol{\sigma}^{(p)} = G \begin{pmatrix} 1/(1 - 2\dot{\epsilon}\tau) & 0 & 0 \\ 0 & 1/(1 + \dot{\epsilon}\tau) & 0 \\ 0 & 0 & 1/(1 + \dot{\epsilon}\tau) \end{pmatrix}.$$

The extensional viscosity is $\mu_e = (\sigma_{11} - \sigma_{22})/\dot{\epsilon}$ and is divergent at $\dot{\epsilon} = 1/(2\tau)$. This divergence of viscosity at a finite strain rate is a consequence of the assumption of a linear force response to distension in the microscopic model. That is, there is no limit to the stretching of polymer coils in the Oldroyd-B model.

That said, recent numerical studies by Thomases and Shelley (2007) suggest that such divergences are only realized exponentially in time, and their singular character is strongly dependent upon the Weissenberg number and the flow geometry. Further, flows associated with polymer stretching in hyperbolic stagnation can undergo symmetry-breaking instabilities at critical values of the Weissenberg number of the flow, and these instabilities can lead to new dynamical states associated with coherent structures and fluid mixing (Arratia *et al.* 2006; Thomases and Shelley 2009).

The Oldroyd-B model is one of the simplest models of a viscoelastic fluid that is derived from microscopic principles. It has the advantage of being closed at the macroscopic level, but it is limited by the absence of shear thinning and, more notably, by the lack of a limit on polymer distension. FENE (finitely extensible nonlinear elastic spring) models overcome the latter shortcoming by using a nonlinear spring law that diverges at a finite distension length. However, FENE models do not generally close at the macroscopic level, requiring the evolution of a Smoluchowski equation at every point in the domain. A commonly used closure approximation is the so-called FENE-P model, which replaces $\text{tr}(\mathbf{R}\mathbf{R}^{\text{T}})$ in the nonlinear force law by $\text{tr}\langle\mathbf{R}\mathbf{R}^{\text{T}}\rangle$. Other models with different transport operators and nonlinearities include the Johnson–Segalman model and the Giesekus model (Larson 1995).

3.4   Applications

Owing to the wide range of elastic moduli (0.1–10Pa), viscosities (0.1–10Pa s), and relaxation times (1–10 s) (Lauga 2007; Smith *et al.* 2009), relating complex biological fluids to viscoelastic flow models can be challenging. We focus now on two applications, peristaltic pumping and swimming, which illustrate the effect of viscoelasticity upon these fundamental means of biological transport. The examples show complex

78   *Dynamics of complex biofluids*

dynamical behavior fundamentally different from that in a Newtonian fluid, and fall into the broad category of complex biofluids.

3.4.1   Pumping a viscoelastic fluid

We start by first considering peristaltic pumping, which is a fundamental transport mechanism for bulk fluids and materials, in both biological and industrial settings. Peristalsis occurs when contractile waves propagate down a fluid-containing tube and is schematically illustrated in Fig. 3.4a. It is the dominant means of material movement in digestive and reproductive tracts, and can involve complex biofluids such as cervical mucus. Fauci and Dillon (2006) have reviewed this area within the context of reproductive fluid dynamics.

   As already stated, in many biological settings the pumped fluid is non-Newtonian. To study peristaltic pumping of such fluids, Teran *et al.* (2008) developed a numerical method based on the immersed boundary method of Peskin (2002) for the simulation of the Stokes-OB equations in a time-dependent geometry. For boundaries with moving peristaltic waves of deformation (see Fig. 3.4(a), Teran *et al.* showed that viscoelasticity produces fundamentally different results from the Newtonian case. Figure 3.4(b) shows the mean flow rate Θ as a function of the occlusion ratio χ (the ratio of the wave amplitude to the mean channel width; $\chi = 1$ means complete occlusion), for various Weissenberg numbers. The flow rate Θ was computed at long times in order to remove the effect of the particular initial data for the polymer extra stress. For small Weissenberg numbers, Θ increases monotonically with χ in a fashion similar to that for a Newtonian fluid, albeit with smaller values. For larger Weissenberg numbers, the flow rate reaches its maximum and then declines, well before complete occlusion occurs. In short, viscoelasticity can significantly limit pumping by peristalsis.
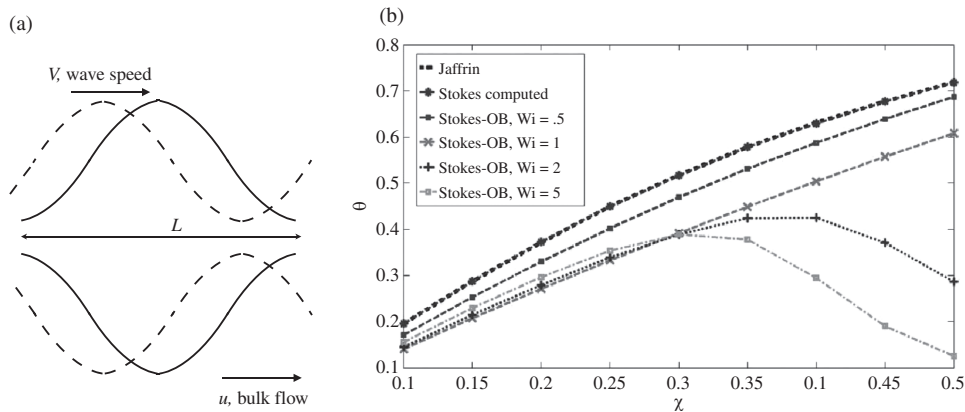

Fig. 3.4   (a) A peristaltic wave of wall deformation propagates with speed V down a channel in the direction of the bulk fluid flow. (b) The dimensionless mean flow rate Θ as a function of the wave amplitude ratio χ and Weissenberg number *Wi*. The upper curve compares the asymptotic result of Jaffrin and Shapiro (1971) with a Newtonian Stokes simulation (second curve from top). The other curves are for nonzero *Wi*. Reproduced with permission from Teran *et al.* (2008).
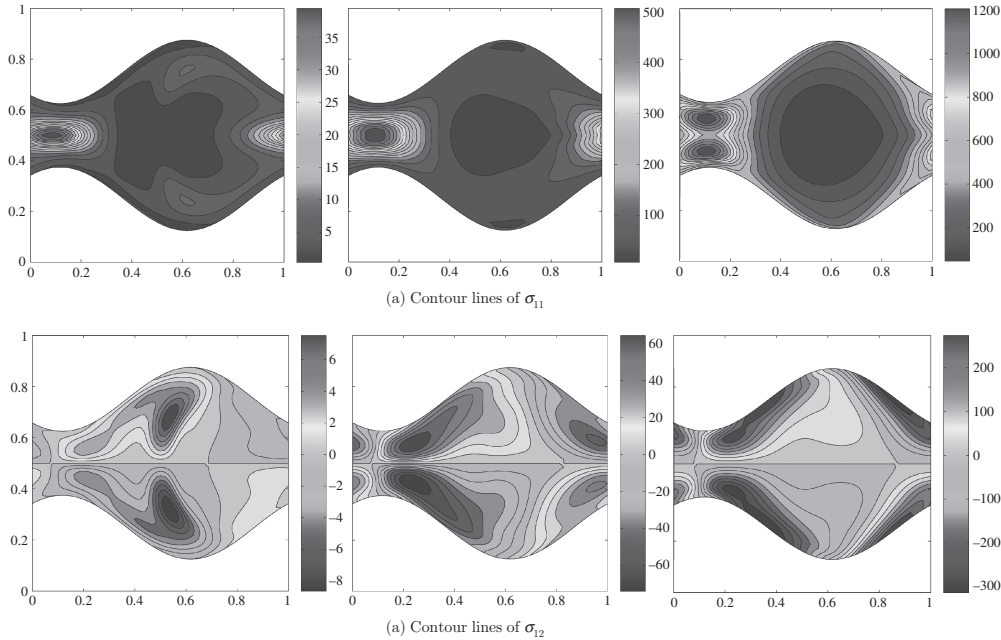
Fig. 3.5 Contours of the polymer stress components at $t_0 = 0.63$, $t_1 = t_0 + 2$, and $t_2 = t_0 + 9$, for $Wi = 5$ and $\chi = 0.5$. The peristaltic wave moves from right to left. Reproduced with permission from Teran *et al.* (2008).

As an illustrative example of the dramatic effects of viscoelasticity, Fig. 3.5, from Teran *et al.* (2008), shows the evolving polymer stress components σ_{11} and σ_{12} from simulations with $Wi = 5$ and $\chi = 0.5$. Unlike the case of a Newtonian Stokes flow, the material stresses now show strong time dependencies, and develop asymmetries that are associated with flow irreversibility. Over time, the viscoelastic polymer stresses also develop strong gradients in the neighborhood of the pump neck, and these structures are implicated in the strong viscoelastic refluxes that can inhibit pumping at even moderate occlusion ratios.

3.4.2   Swimming

The study of undulatory swimming at low Reynolds number in Newtonian fluids dates back to classical work by Taylor (1951), Lighthill (1960), and Purcell (1977). This continues to be a very active area, and recent example studies include those by Tam and Hosoi (2007) and Spagnolie and Lauga (2010), who both studied optimization of swimming strokes for speed and efficiency in a Newtonian fluid. In the Newtonian regime, there are a wealth of numerical and analytical tools, such as singularity and boundary integral methods that reduce representations of three-dimensional Stokes flows to two- or even one-dimensional problems; see Pozrikidis (1992). As with peristaltic pumping, the situation is more difficult when one studies the effect of viscoelasticity upon swimming.

3.4.2.1 *Swimming sheet*

For the Newtonian case, an analysis of swimming by a periodic bi-infinite sheet was provided by Taylor (1951), who performed a small-amplitude analysis and showed that with a sinusoidal deformation of amplitude A, the swimming speed scaled like $O(A^2)$. This problem was reexamined by Lauga (2007) for the viscoelastic case. He considered solutions that are steady in the traveling-wave frame, found the same small-amplitude scaling as Taylor, and showed that a swimmer in a Newtonian Stokes fluid was always faster than a Stokes-OB swimmer. A similar study was performed by Fu *et al.* (2007, 2009) for small-amplitude flagellar swimming.

To study the influence of viscoelasticity on the speed and efficiency of undulatory swimming in the time-dependent, large-amplitude case, Teran *et al.* (2010) developed a numerical model, based on the immersed boundary method of Peskin (2002), for the swimming of an undulating sheet immersed in a Stokes-OB fluid. The immersed sheet is an effectively inextensible surface along which a traveling bending wave moves. Wave motion is induced through an immersed boundary force derived from an elastic energy with a time-dependent preferred curvature (Fauci and Peskin 1988).

For small amplitudes and doubly periodic sheets, Teran *et al.* (2010) recovered the Taylor/Lauga scaling of swimming speed. Moreover, they found that as the amplitude increased, the Newtonian swimmer (i.e. an infinite sheet in a Newtonian liquid) was always faster than an Oldroyd-B swimmer, as predicted by Lauga (2007).

If the sheet is allowed to have a head and a tail, i.e. is a free swimmer, these results change drastically at large amplitudes. Figure 3.6(a) shows the horizontal displacement of the center of mass of the swimmer for varying De with $\beta = 1/2$, for a swimming stroke whose amplitude increases towards the tail, as is typical of sperm locomotion. Since the initial data for the polymer stress was the identity in all cases, all swimmers start off at the same speed. However, at long times, the swimming speeds rearrange themselves and reveal that the fastest swimmer has an $O(1)$ Deborah number. Figure 3.6(b) shows the fastest swimmer ($De = 1$), the slowest ($De = 5$, the largest value considered), and the Newtonian case, at the final time $t = 20$. Despite the substantially slower speed of the $De = 5$ swimmer, it is almost tied with the Newtonian free swimmer at this final time owing to its faster swimming speed at intermediate times.

Figure 3.7 shows graphically the distension of the polymer stress field at late times for the fastest swimmer ($De = 1$). In Fig. 3.7a, the free swimmer is very near the time of peak forward velocity during its stroke, when the backward moving wave has approached the tail, which is itself moving slightly upwards. Owing to the strong straining of the fluid by the motion of the tail, there is a large concentration of polymer stress concentration aft of the swimmer. Figure 3.7(b) is about one-quarter of a stroke later. The stress is now much more anisotropic, and the swimmer is actually slipping backwards. However, in comparison with the Newtonian case, the backwards slippage is of smaller magnitude, leading to an overall faster swimmer.

Note that these results for large-amplitude free swimmers are different from those of Lauga (2007) for small-amplitude periodic sheets. In particular, the study of Teran *et al.* (2010) predicts that both swimming speed and efficiency are maximized at a Deborah number of $O(1)$, when the stroke period is nearly matched to the relaxation
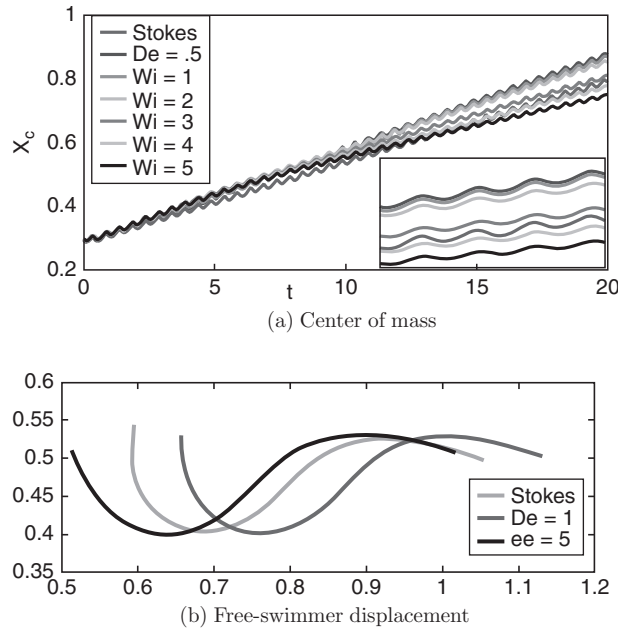
(a) Center of mass

(b) Free-swimmer displacement

Fig. 3.6 (a) The location of the x-component of the center of mass of a free swimmer with $A = 0.05$ and various values of De. Inset: long-time behavior. (b) Shape and displacement of three free swimmers ($De = 0, 1, 5$) after 20 periods. Reproduced with permission from Teran *et al.* (2010).

time of the fluid. These results seem to be in qualitative agreement with recent experimental work of Smith *et al.* (2009), who found that human spermatozoa swim at a Deborah number of $O(1)$ in synthetic cervical mucus, and show greater displacement per stroke than in less viscoelastic media.

3.4.2.2   *Active suspensions of swimming rods*

The previous example considered the locomotion of single microswimmers in a viscoelastic fluid and showed the fundamental differences from locomotion in a Newtonian fluid. We now address instead the collective hydrodynamics of many active swimmers in a Newtonian fluid, i.e., an active suspension. Experiments by Kessler, Goldstein, and co-workers (Dombrowski *et al.* 2004; Tuval *et al.* 2005; Sokolov *et al.* 2007) showed that in the case of concentrated bacterial baths, large-scale vortices and jets emerged. These flow features were reproduced qualitatively by Graham and co-workers (Hernández-Ortiz *et al.* 2005; Underhill *et al.* 2008), using a force-dipole (dumbbell) model, and by Saintillan and Shelley (2007) using a more detailed model of the rod-like swimmer described in Example 4. Figure 3.8 shows a particle simulation from Saintillan and Shelley (2007) of 2500 Pusher particles (rods) in a box of size $10 \times 10 \times 3$ (in units of particle length). Initially, the rods are aligned, though with
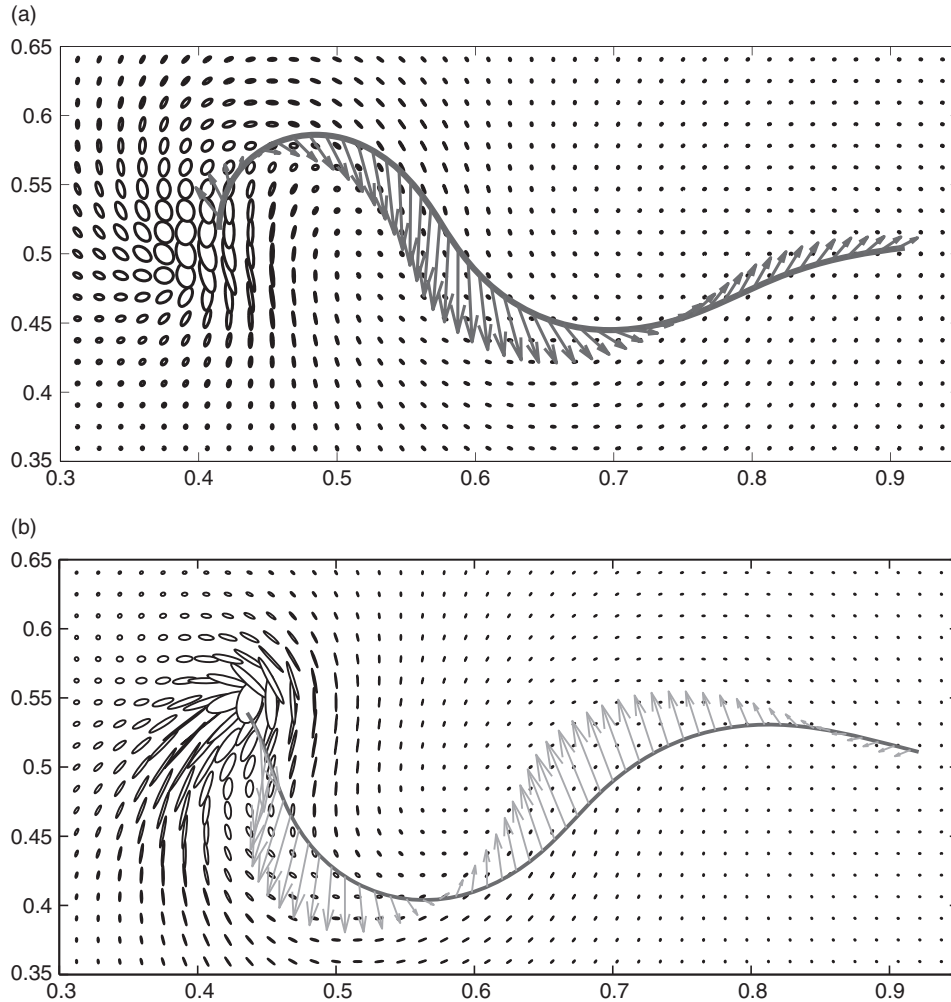
Fig. 3.7 Distension of polymer stress field by a free swimmer with $De = 1$ at late times. The ellipses represent $\boldsymbol{\sigma}$; the major axis is aligned with the principal eigenvector of $\boldsymbol{\sigma}$, with its length scaled by the associated eigenvalue, and the minor axis is associated with the second eigenvector. The vectors represent the fluid velocity on the swimmer. Reproduced with permission from Teran *et al.* (2010).

randomly chosen positions. As time increases, instabilities develop that move the rods away from global alignment, and eventually there emerge system-scale vortices and jets that are reminiscent of the experimental observations of Kessler, Goldstein, and co-workers (Dombrowski *et al.* 2004; Tuval *et al.* 2005; Sokolov *et al.* 2007). Although the initial global orientational order is destroyed, the subsequent dynamics preserves the local alignment of co-swimming particles over about a body length. Whereas the
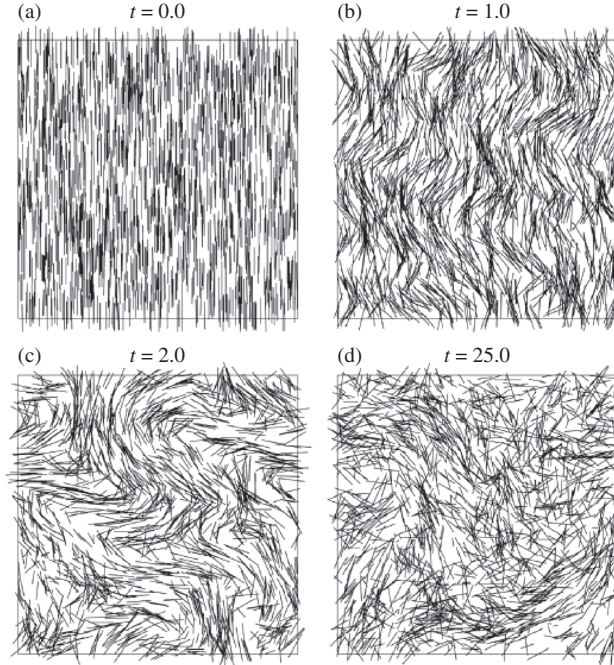
Fig. 3.8 Particle simulation of 2500 initially aligned Pushers in a box of size $10 \times 10 \times 3$ (in units of particle length) at an effective volume fraction $\tilde{\nu} = \nu/8 = 1$, showing the different stages of the dynamics (a)–(d). Reproduced with permission from Saintillan and Shelley (2007).

background flow is on the scale of the system, the individual swimmers show random walk statistics, where the random-walk seems to result from pair interactions, at least at lower volume concentrations. The onset of the large-scale instabilities appears to depend upon the effective volume concentration $\tilde{\nu} = \nu/8$ ($\nu = (Nl^3)/L^3$) of swimmers (see Fig. 2b of Saintillan and Shelley 2007).

Saintillan and Shelley (2008*a,b*) subsequently developed a continuum model to describe large-scale macroscopic phenomena, based on the evolution of the probability distribution function (see Section 3.2), which we now discuss.

The configuration variables of a swimming rod are its center-of-mass position and its orientation. Therefore, the Smoluchowski equation (3.1) becomes

$$\frac{\partial \Psi}{\partial t} = -\nabla_x \cdot (\dot{\mathbf{x}} \Psi) - \nabla_p \cdot (\dot{\mathbf{p}} \Psi). \tag{3.33}$$

The particle fluxes are given by eqns (3.11) and (3.12). Recall that the normalization of Ψ is such that $\int dV_x \int dS_p \Psi = nL^3$:

$$\dot{\mathbf{x}} = U\mathbf{p} + \mathbf{u} - D_p \nabla_x \ln \Psi, \tag{3.34}$$

$$\dot{\mathbf{p}} = (\mathbf{I} - \mathbf{p}\mathbf{p}^{\mathrm{T}}) \cdot \nabla \mathbf{u} \, \mathbf{p} - d_p \nabla_p \ln \Psi. \tag{3.35}$$

84   *Dynamics of complex biofluids*

The background flow satisfies the incompressible Stokes equations, forced by the extra stress generated by the swimming rods:

$$-\mu\Delta_x\mathbf{u} + \nabla_x q = \nabla_x \cdot \boldsymbol{\sigma}, \qquad \nabla_x \cdot \mathbf{u} = 0. \tag{3.36}$$

We consider two broad categories of swimmers: Pushers and Pullers. A Pusher, whose motion is actuated along the posterior of the body, served as motivation in Example 4. In contrast, the motion of a Puller is actuated along the anterior of the body, resulting in an oppositely signed extra-stress contribution (while moving in the same direction). Bacteria such as *B. subtilis* might be described as Pushers, while algae such as *Chlamydomonas* might be roughly described as Pullers. Figure 3.9 illustrates the flow lines for Pushers and Pullers and shows schematic pictures. We remark that there are other swimming microorganisms, such as the multicellular algae *Volvox* and densely covered ciliates, that may not fall into these categories. Following the discussion in Section 3.2, the extra stress for a Pusher is $\boldsymbol{\sigma} = -\sigma_0 \int dS_p(\mathbf{pp}^{\mathrm{T}} - \mathbf{I}/3)\Psi$ (see also eqn (3.23)); for a Puller, $\boldsymbol{\sigma}$ is identical in magnitude but oppositely signed.

To nondimensionalize eqns (3.33)–(3.36), we choose the rescaling $x \to l_c\mathbf{x}$, $\mathbf{u} \to U\mathbf{u}$, $t \to (l_c/U)t$, and $\Psi \to n\Psi$. Here l_c is an intrinsic length scale to be determined. With the appropriate rescaled pressure, we obtain the following for the Smoluchowski equation and particle fluxes:

$$\frac{\partial\Psi}{\partial t} = -\nabla_x \cdot (\dot{\mathbf{x}}\Psi) - \nabla_p \cdot (\dot{\mathbf{p}}\Psi), \tag{3.37}$$

$$\dot{\mathbf{x}} = \mathbf{p} + \mathbf{u} - D\nabla_x \ln\Psi, \tag{3.38}$$

$$\dot{\mathbf{p}} = (\mathbf{I} - \mathbf{pp}^{\mathrm{T}})\nabla_x\mathbf{u}\,\mathbf{p} - d\nabla_p \ln\Psi. \tag{3.39}$$

The forced Stokes equations become

$$-\Delta\mathbf{u} + \nabla q = \nabla \cdot \boldsymbol{\Sigma}^a, \qquad \nabla_x \cdot \mathbf{u} = 0, \tag{3.40}$$

$$\boldsymbol{\Sigma}^a = \alpha \int dV_x \int dS_p\,(\mathbf{pp}^{\mathrm{T}} - \mathbf{I}/3)\Psi. \tag{3.41}$$

The nondimensional constants are $D = D_p/(l_cU_0)$, $d = d_p l_c/U_0$, $\tilde{L} = L/l_c$, and $\alpha = -(l_c\sigma_0 n)/(\mu U_0)$.
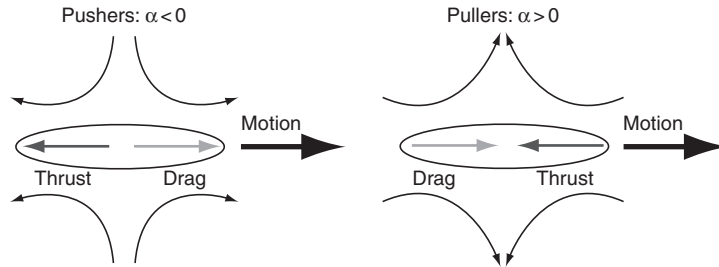

Fig. 3.9 Flow lines for Pushers ($\alpha < 0$) and Pullers ($\alpha > 0$).

To determine l_c, we rewrite α using the expressions for σ_0 and U derived in Examples. 7 and 4, respectively, $\sigma_0 = \kappa_1 l^3 g$ and $U = \kappa_2 lg/\mu$. With these substitutions and $\nu = (Nl^3)/L^3$ for the volume concentration, we obtain $\alpha = -(l_c\nu/l)(\kappa_1/\kappa_2)$. Choosing $l_c = l/\nu$ turns α into a purely geometric constant, $\alpha = -\kappa_1/\kappa_2$.

In their particle simulations of rod-like swimmers, Saintillan and Shelley (2007) observed that at low volume concentrations (up to effective volume concentrations somewhat greater than $\tilde{\nu} = \nu/8 = 1$) $d_p \approx \nu \bar{d}_p$ and $D_p \approx \nu^{-1} \bar{D}_p$. If we assume these observed scalings of d_p and D_p with ν, the nondimensional diffusion coefficients become

$$d = \frac{l\bar{d}_p}{U_0} \quad \text{and} \quad D = \frac{\bar{D}_p}{lU_0}.$$

That is, d and D depend only upon the speed and length, of the swimmer, and the system size and the volume concentration of swimmers appear only in the normalized system size $\tilde{L}$.

We are interested in the nonlinear dynamics of this system, of partial differential equations, and its stability around simple steady states. Before getting into the specifics, we introduce the configurational entropy, which is a natural measure of the fluctuations in this system. The relative configurational entropy is defined as $\mathcal{S} = \int dV_x \int dS_p \, (\Psi/\Psi_0) \ln(\Psi/\Psi_0)$, where Ψ_0 is the constant value taken by Ψ when the system is uniform and isotropic (no concentration or orientation fluctuations). This quantity has the following properties:

1. $\mathcal{S} \geq 0$, and $\mathcal{S} = 0$ if and only if $\Psi \equiv \Psi_0$. That is, a nonzero $\mathcal{S}$ measures the size of the fluctuations away from uniform isotropy, realized when $\Psi = \Psi_0$.
2. The entropy evolves via

$$\Psi_0 \dot{\mathcal{S}} = -\frac{6}{\alpha} \int dV_x \, \mathbf{E} : \mathbf{E} - \int dS_p \int dV_x \Psi \left[D|\nabla_x \ln \Psi|^2 + d|\nabla_p \ln \Psi|^2 \right],$$

   where $\mathbf{E}$ is the symmetric rate-of-strain tensor. The first term on the right-hand side is proportional to the rate of viscous dissipation, and the second is strictly negative and reflects diffusional processes which serve to drive $\mathcal{S}$ towards its minimum (the uniform and isotropic state). The scalings of the system used here give $\Psi_0 = 4\pi$.

We omit the proofs, which are straightforward, of these statements.

The configurational entropy and its evolution establish the uniform isotropic state as a natural steady state to be examined for this system. Given their relevance to the study of biological flocking, the stability of aligned suspensions has also been examined, by Simha and Ramaswamy (2002) and by Saintillan and Shelley (2007, 2008a,b), among others. These authors find that aligned suspensions are generically unstable, particularly in the absence of diffusional processes, regardless of swimmer type (Pusher or Puller). Here we focus on the stability of the uniform isotropic state, which relates naturally to measures of fluctuations in the system, and whose analysis reveals strong differences depending on swimmer type and geometry.

86   *Dynamics of complex biofluids*

We now turn our attention to the details of the stability of a uniform, isotropic suspension of active swimmers. First, some general conclusions can be drawn from Property 2 of the configurational entropy. For suspensions of Pullers, where $\alpha > 0$, we have $\dot{\mathcal{S}} < 0$, and fluctuations away from the uniform, isotropic state are expected to decay. On the other hand, for Pushers ($\alpha < 0$), the leading term is now positive, which allows the possibility of fluctuation growth and eventual balance with diffusion. Furthermore, if there is no diffusion, fluctuations should grow. These issues were analyzed in a detailed study of a system linearized near uniform isotropy (Hohenegger and Shelley 2010).

Let $\Psi = 1/(4\pi)\,(1 + \varepsilon\psi)$, $\mathbf{v} = \varepsilon\mathbf{u}$, and $q \to \epsilon q$ with $\varepsilon \ll 1$. Keeping only linear-order terms and using the identity $\nabla_p \cdot (f_1\hat{\theta} + f_2\hat{\phi}) = (1/\sin\phi)(\partial_\theta f_1 + \partial_\phi(\sin\phi f_2))$, eqns (3.37)–(3.41) become

$$\psi_t + \mathbf{p} \cdot \nabla_x\psi - 3\mathbf{p}\mathbf{p}^{\mathrm{T}} : \nabla_x\mathbf{u} = D\nabla_x^2\psi + d\nabla_p^2\psi, \tag{3.42}$$

$$-\Delta_x\mathbf{u} + \nabla_x q = \nabla_x \cdot \boldsymbol{\sigma}, \qquad \nabla_x \cdot \mathbf{u} = 0, \tag{3.43}$$

where $\boldsymbol{\sigma} = (\alpha/4\pi) \int dS_p\,\psi\,(\mathbf{p}\mathbf{p} - \mathbf{I}/3)$.

The first step of the stability analysis is to transform the equations using a spatial Fourier transform in $\mathbf{x}$, $\tilde{f}_k = \int dV\,e^{-i\mathbf{k}\cdot\mathbf{x}}f(\mathbf{x})$, to decouple eqns (3.42) and (3.43) in the wave vector $\mathbf{k}$ ($k = |\mathbf{k}|$, $\mathbf{k} = k\hat{\mathbf{k}}$). From eqn (3.43), $\tilde{\mathbf{u}}_k = (i/k)(\mathbf{I} - \hat{\mathbf{k}}\hat{\mathbf{k}}^{\mathrm{T}}) \cdot \tilde{\boldsymbol{\sigma}}_k \cdot \hat{\mathbf{k}}$, and eqn (3.42) then becomes

$$\partial_t\tilde{\psi}_k = -ik\hat{\mathbf{k}} \cdot \mathbf{p}\,\tilde{\psi}_k - Dk^2\tilde{\psi}_k + d\nabla_p^2\tilde{\psi}_k - 3\mathbf{p}\mathbf{p}^{\mathrm{T}} : (\mathbf{I} - \hat{\mathbf{k}}\hat{\mathbf{k}}^{\mathrm{T}}) \cdot \tilde{\boldsymbol{\sigma}}_k \cdot \hat{\mathbf{k}}\hat{\mathbf{k}}. \tag{3.44}$$

The explicit dependence of eqn (3.44) on the direction of $\hat{\mathbf{k}}$ can be removed by a rotation, $\hat{\mathbf{k}} = \mathbf{R}\mathbf{z}$, which defines $\mathbf{q}$ through $\mathbf{p} = \mathbf{R}\mathbf{q}$. Let $\theta \in [0, 2\pi]$ be the azimuthal angle and let $\phi \in [0, \pi]$ be the polar angle on the unit $\mathbf{q}$-sphere. Equation (3.44) then becomes

$$\partial_t\tilde{\psi}_k = -ik\cos\phi\,\tilde{\psi}_k - Dk^2\tilde{\psi}_k + d\nabla_q^2\tilde{\psi}_k - 3\cos\phi\,\mathbf{q} \cdot (\mathbf{I} - \hat{\mathbf{z}}\hat{\mathbf{z}}^{\mathrm{T}}) \cdot \mathbf{R}^{\mathrm{T}} \cdot \tilde{\boldsymbol{\sigma}}_k \cdot \mathbf{R} \cdot \mathbf{z}.$$

A further decoupling in θ is achieved by introducing a Fourier series in θ, $\tilde{\psi}_k = \sum_n A_{n,k}(\phi, t)e^{in\theta}$. After some algebra, we find

$$\partial_t A_{n,k} + A_{n,k}\left(ik\cos\phi + Dk^2\right) + d\left(\frac{n^2}{\sin^2\phi}A_{n,k} - \frac{1}{\sin\phi}\partial_\phi(\sin\phi\,\partial_\phi A_{n,k})\right)$$
$$= -\frac{3\alpha}{4}\cos\phi\sin\phi\,F[A_{n,k}]\delta_{n,1}, \tag{3.45}$$

where the scalar operator F is

$$F[h] = \int_0^\pi d\phi'\,h(\phi')\sin^2\phi'\cos\phi'$$

and $\delta_{n,1}$ is the Kronecker delta symbol.

The main feature of eqn (3.45) is that the entire stability is controlled by the first azimuthal mode on the sphere.

We now look for exponential solutions to eqn (3.45) in the special case when $D = d = 0$ and $\alpha < 0$ (Pushers). Hence we assume that $A_{1,k}(\phi, t) = \gamma_k(\phi)e^{\sigma t}$ and note that there is no a priori expectation that $A_{1,k}$ can be represented in this fashion, as eqn (3.45) depends explicitly on ϕ. Nonetheless, inserting the exponential ansatz into eqn (3.45) and applying F to both sides yields the eigenvalue relation

$$-\frac{3}{4}\alpha \int_0^\pi d\phi' \frac{\sin^3 \phi' \cos^2 \phi'}{\sigma + ik\cos\phi'} = 1. \tag{3.46}$$

This complex-valued integral can be evaluated by substitution and separation into real and imaginary parts. Some algebra produces the complex equation

$$-\alpha \left[4i\sigma k^3 + 6i\sigma^3 k - 3\sigma^2(\sigma^2 + k^2)\ln\frac{i\sigma - k}{i\sigma + k} \right] = 4ik^5, \tag{3.47}$$

where the complex logarithm is defined as $\ln(a + ib) = \ln\sqrt{a^2 + b^2} + i\arctan(b/a)$. Note that eqn (3.47) is valid only if $Re(\sigma) \neq 0$. Figure 3.10 shows a numerical solution of eqn (3.47), plotting the real and imaginary parts of σ for $\alpha = -1$. For small k, there are two branches of unstable eigenvalues with zero imaginary part, and the decrease in growth rate suggests a crossing of the k-axis to become negative at medium k. Saintillan and Shelley (2008b) gave an asymptotic solution for $k \ll 1$ for the upper branch in Fig. 3.10,

$$\sigma(k) = -\frac{\alpha}{5} + \left[\frac{15}{7\alpha} - D \right] k^2 + O(k^3). \tag{3.48}$$

For a suspension of Pushers ($\alpha < 0$), eqn (3.48) implies the existence of a long-wave instability with $\lim_{k\to 0}\sigma(k) = -\alpha/5 > 0$, corresponding to the upper branch in Fig. 3.10. In contrast, for Pullers, there is no long-wave instability.
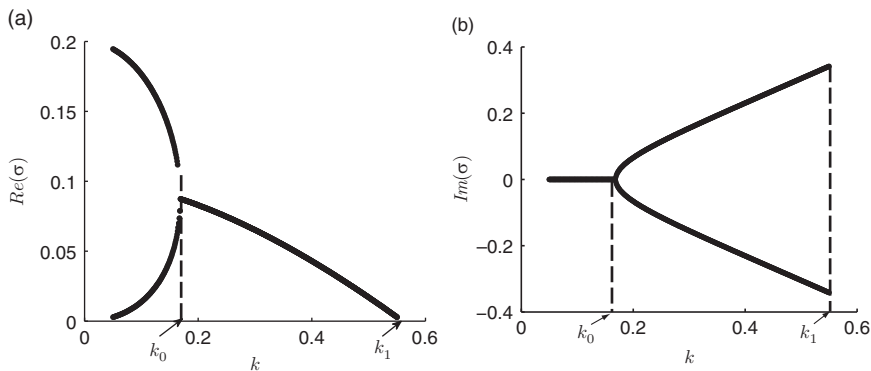

Fig. 3.10 Real and imaginary parts of the growth rate $\sigma(k)$ for $\alpha = -1$ (Pushers) with $D = d = 0$. Reproduced with permission from Hohenegger and Shelley (2010).

88   *Dynamics of complex biofluids*

One of the striking features of the analysis of the eigenvalue problem (Hohenegger and Shelley 2010) is that there is no crossing to negative k, contrary to the intuition gathered from Fig. 3.10. As a matter of fact, a singular behavior develops in the corresponding eigenvector as k approaches k_1, the zero-growth-rate value. The singular behavior results from a discontinuous pole singularity in the integral in eqn (3.46) as $Re(\sigma)$ approaches 0.

Finally, we remark that if $k = k_1$ is indeed a point of stability transition, then there exists a critical system size L or volume concentration ν above which the system becomes unstable. This follows from having scaled by the intrinsic length l_c, so that $k_1' = (k_1/2\pi)(\nu L/l)$. As the first allowable mode in the periodic box has $k' = 1$, the system is unstable if $k_1' \approx 0.089(\nu L/l) > 1$, and is stable otherwise.

As just highlighted, the eigenvalue analysis does not provide solutions for $k > k_1$. The dynamics in these cases was found numerically and was confirmed by a large k analysis (Hohenegger and Shelley 2010). Figure 3.11 illustrates these numerically determined solutions in the absence of diffusion. In each case, the initial condition is $A_{1,k}(\phi, 0) = \sin(\phi)$. In Fig. 3.11, the real and imaginary parts of $A_{1,k}$ for $k = 0.4$, $k = 0.8$, and $k = 10$ are plotted at $t = 50$ and $t = 100$ for Pushers ($\alpha = -1$). For $k = 0.4$, the real and imaginary parts (Fig. 3.11(a)) grow as predicted by the eigenvalue analysis. The values $k = 0.8$ and $k = 10$ are out of the range of exponential growth and both the real and the imaginary parts of the solution show oscillations. The number of oscillations increases with time, as illustrated with Figs. 3.11(b) and (c), and Fig. 3.11(d) shows that for large k, the envelope of the oscillations is determined by the initial condition (and is as determined analytically by Hohenegger and Shelley 2010).

We expect rotational diffusion (i.e. $d > 0$) to remove the singular behavior in the eigenvalue problem, and to yield exponentially decaying solutions past a crossing value. To investigate this, we assume again that $A_{1,k}(\phi, t) = \gamma_k(\phi)e^{\sigma t}$ in eqn (3.45) and renormalize the problem so that $F[\gamma_k] = 1$. Upon substitution into eqn (3.45), this leads to the system

$$\gamma_k(\sigma + ik\cos\phi + Dk^2) + d\left(\frac{1}{\sin^2\phi}\gamma_k - \frac{1}{\sin\phi}\partial_\phi\left(\sin\phi\,\partial_\phi\gamma_k\right)\right) = -\frac{3\alpha}{4}\cos\phi\sin\phi,$$

$$(3.49)$$

$$\int_0^\pi d\phi'\gamma_k(\phi', t)\sin^2\phi\cos\phi = 1. \qquad (3.50)$$

Equations (3.49) and (3.50) were solved by discretizing the ϕ-derivatives and solving the resulting nonlinear system via Newton iteration starting from the known solution for $d = 0$.

In Fig. 3.12, the real part of $\sigma(k)$ obtained from eqns (3.49) and (3.50) with $d = 0$ and $d = 0.01$ is plotted. For this moderate degree of rotational diffusion, a downward shift of the branches is seen, leaving the long-wave instability intact but suppressing the lower branch. Not only does rotational diffusion reduce growth rates, but it also suppresses the eigenfunction singularity. For a suspension of Pullers, there are no positive growth rates for $d \geq 0$, as would be expected from the generic decay of the entropy.
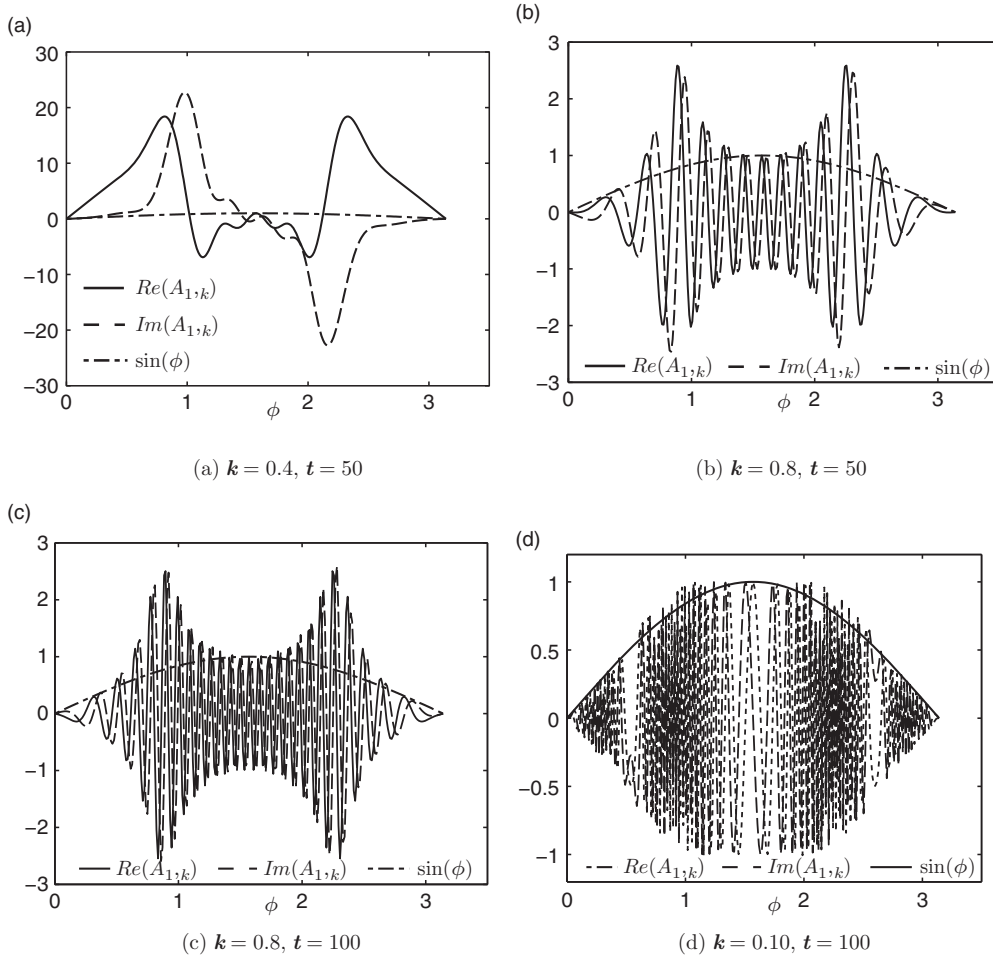
Fig. 3.11 Real and imaginary parts of the first Fourier modes $A_{1,k}(\phi, t)$ for $\alpha = -1$ (Pushers) and $D = d = 0$, from a single-mode sinusoidal initial condition. The increasing wavenumbers k show growth (top left), saturation in amplitude with an increasing number of oscillations in time (top right and bottom left), and convergence of the wave envelope to that of the initial condition. Reproduced with permission from Hohenegger and Shelley (2010).

The theoretical considerations above allow a comparison with the rod simulations of Saintillan and Shelley (2007). First, we remark that for saintillan and shelley's rod model, we estimate $\alpha \approx -0.9$, close to the value of -1 that we have used in the theoretical study described above. Using values for $\bar{d}_p$ and $\bar{D}_p$ gleaned from Saintillan and Shelley (2007), we have solved the eigenvalue problem of eqns (3.49) and (3.50). This yields the crossing value $k_1 \approx 0.086$, and hence instability is found if $k_1' = (k_1/2\pi)(\nu L_p/l) > 1$. Taking $l = 1$ and $L_p = 10$, this analysis predicts the existence of a critical volume concentration $\tilde{\nu} = 0.9$ ($\tilde{\nu} = \nu/8$) for the emergence of a
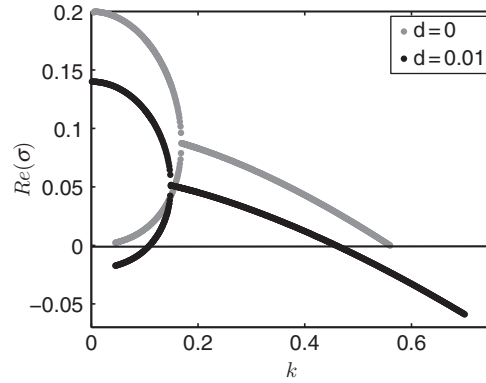
Fig. 3.12   Continuation of the real part of the growth rate $\sigma(k)$ for positive rotational diffusion $d = 0.01$, $\alpha = -1$ (Pushers), and $D = 0$. Reproduced with permission from Hohenegger and Shelley (2010).
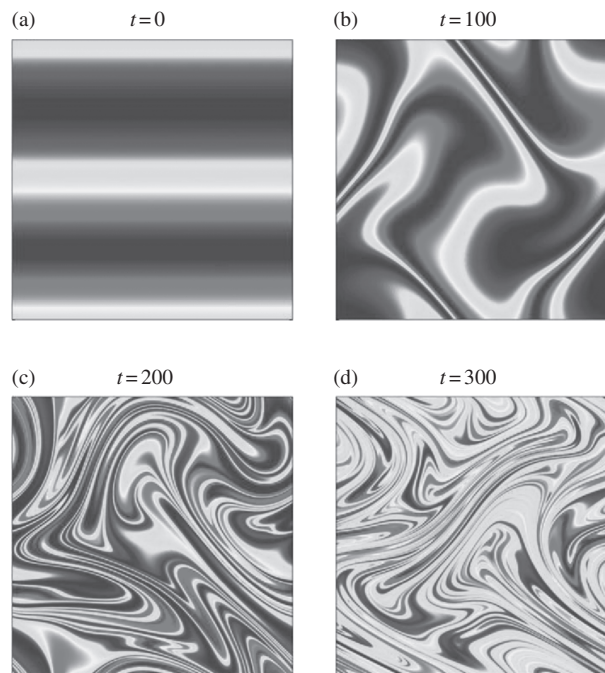

Fig. 3.13   Fluid mixing by an active suspension of Pushers ($\alpha = -1$). The gray levels show the configuration of a passive scalar field in the suspension at different times. Reproduced with permission from Saintillan and Shelley (2008*b*).

long-wave instability. This is consistent with the result of Saintillan and Shelley (2007) that organized dynamics emerges at volume concentrations in the neighborhood of $\tilde{\nu} = 0.5$.

Using kinetic theory, Saintillan and Shelley (2008a,b) simulated this instability starting from uniform isotropy in the special case of two-dimensional flows. Figure 3.13 shows the evolution away from uniform isotropy through the dynamics of a scalar field being advected by the background velocity field. The fully developed nonlinear dynamics is quasi-periodic, has persistent concentration fluctuations (not predicted by linear theory), and yields efficient mixing of the scalar field through repeated folding and stretching of fluid elements. It was also found that the system reached a state of statistical equilibrium where the growth of configurational entropy saturates and where fluctuation growth is balanced, on average, by diffusional processes.

3.5   Conclusions

In our lectures and in these notes, we have reviewed the basics of non-Newtonian fluid mechanics and established formulae for the extra-stress contribution to the macroscopic stress tensor, in the particular cases of dumbbell- and- rod shaped particles. We discussed the derivation and properties of the Oldroyd-B model. We then focused on pumping and swimming in viscoelastic fluids as important biological examples. Both of these problems concern complex fluid–body interactions and required the development and use of sophisticated numerical methods (which we did not discuss in any detail). We then developed and analyzed the continuum theory of active particle suspensions put forward by Saintillan and Shelley (2008a,b), focusing on its structure near a state of uniform isotropy.

There are of course many other fascinating problems which could have been discussed if time had allowed. Among many such examples are the study of synthetic swimmers (e.g. Zerrouki *et al.* 2008; Keaveny and Shelley 2009), and microfluidic pumps produced by carpets of bacteria bound to channel walls (Kim and Breuer 2008).

Similarly, there are many directions in which the problems discussed here can evolve. We conclude by briefly mentioning some of these. Peristaltic pumping was shown to be hindered by viscoelasticity. Therefore a natural question to ask pertains to the optimal wave shape that minimizes the input power. Walker and Shelley (2010) developed a shape optimization algorithm for the Newtonian case, but the extension to a viscoelastic fluid is open. The continuum model of swimming rods gave rise to complex large-scale behavior, but the linearized analysis around uniformity and isotropy did not show growth in concentration fluctuations (on the contrary, these decayed). Furthermore, it is believed that in bacterial baths, other effects such as chemotaxis or oxygen-taxis (Sokolov *et al.* 2007), which were not included here, can play a significant role. Finally, motile microorganisms such as bacteria also thrive and move in other yet more complicated media, such as gel-like soft tissues and mucus.

Acknowledgments

References

Arratia P. E., Thomas C. C., Diorio J., and Gollub J. P. (2006). Elastic instabilities of polymer solutions in cross-channel flow. *Physical Review Letters*, **96**, 144502.

Batchelor G. K. (1970*a*). The stress system in a suspension of force-free particles. *Journal of Fluid Mechanics*, **41**, 545–570.

Batchelor G. K. (1970*b*). Slender-body theory for particles of arbitrary cross-section in Stokes flow. *Journal of Fluid Mechanics*, **44**, 419–440.

Batchelor G. K. (1977). The effect of Brownian motion on the bulk stress in a suspension of spherical particles. *Journal of Fluid Mechanics*, **83**, 97–117.

Bird R. B., Armstrong R. C., and Hassager O. (1987). *Dynamics of Polymeric Fluids: Kinetic Theory*. Wiley.

Doi M. and Edwards S. F. (1986). *The Theory of Polymer Dynamics*. Oxford University Press.

Dombrowski C., Cisneros L., Chatkaew S., Goldstein R. E., and Kessler J. O. (2004). Self-concentration and large-scale coherence in bacterial dynamics. *Physical Review Letters*, **93**, 098103.

Fauci L. J. and Peskin C. S. (1988). A computational model of aquatic animal locomotion. *Journal of Computational Physics*, **77**, 85–108.

Fauci L. J. and Dillon R. (2006). Biofluidmechanics of reproduction. *Annual Review of Fluid Mechanics*, **38**, 371–394.

Fu H. C., Powers T. R., and Wolgemuth C. W. (2007). Theory of swimming filaments in viscoelastic media. *Physical Review Letters*, **99**, 258101.

Fu H. C., Wolgemuth C. W., and Powers T. R. (2009). Swimming speeds of filaments in nonlinearly viscoelastic fluids. *Physics of Fluids*, **21**, 033102.

Groisman A. and Quake S. R. (2004). A microfluidic rectifier: Anisotropic flow resistance at low Reynolds numbers. *Physical Review Letters*, **92**, 094501.

Groisman A. and Steinberg V. (2001). Efficient mixing at low Reynolds numbers using polymer additives. *Nature*, **410**, 905–908.

Groisman A. and Steinberg V. (2004). Elastic turbulence in curvilinear flows of polymer solutions. *New Journal of Physics*, **6**, 29.

Hernández-Ortiz J. P., Stolz C. G., and Graham M. D. (2005). Transport and collective dynamics in suspensions of confined swimming particles. *Physical Review Letters*, **95**, 204501.

Hohenegger C. and Shelley M. J. (2010). Stability of active suspensions. *Physical Review E*, **81**, 046311.

Jaffrin M. and Shapiro A. (1971). Peristaltic pumping. *Annual Review of Fluid Mechanics*, **3**, 13.

Jeffery G. B. (1922). The motion of ellipsoidal particles immersed in a viscous fluid. *Proceedings of the Royal Society of London*, **102**, 161–179.

Johnson R. E. (1980). An improved slender-body theory for Stokes-flow. *Journal of Fluid Mechanics*, **99**, 411–431.

Keaveny E. E. and Shelley M. J. (2009). Hydrodynamic mobility of chiral colloidal aggregates. *Physical Review E*, **79**, 051405.

Keller J. B. and Rubinow S. I. (1976). Slender-body theory for slow viscous-flow. *Journal of Fluid Mechanics*, **75**, 705–714.

Kim M. J. and Breuer K. S. (2008). Self-organizing bacteria-powered microfluidic pump. *Small*, **4**, 111–118.

Larson R. G. (1995). *The Structure and Rheology of Complex Fluids*. Oxford University Press.

Lauga E. (2007). Propulsion in a viscoelastic fluid. *Physics of Fluids*, **19**, 081304.

Lighthill M. J. (1960). Note on the swimming of slender fish. *Journal of Fluid Mechanics*, **9**, 305–317.

Paxton W. F., Kistler K. C., Olmeda C. C., Sen A., St. Angelo S. K., Cao Y., Mallouk T. E., Lammert P. E., and Crespi V. H. (2004). Catalytic nanomotors: Autonomous movement of striped nanorods. *Journal of the American Chemical Society*, **126**, 13424.

Peskin C. (2002). The immersed boundary method. *Acta Numerica*, **11**, 479.

Pozrikidis C. (1992). *Boundary Integral and Singularity Methods for Linearized Viscous Flow*. Cambridge University Press.

Purcell E. M. (1977). Life at low Reynolds number. *American Journal of Physics*, **45**, 11.

Saintillan D. and Shelley M. J. (2007). Orientational order and instabilities in suspensions of self-locomoting rods. *Physical Review Letters*, **99**, 058102.

Saintillan D. and Shelley M. J. (2008*a*). Instabilities and pattern formation in active particle suspensions: Kinetic theory and continuum simulations. *Physical Review Letters*, **100**, 178103.

Saintillan D. and Shelley M. J. (2008*b*). Instabilities, pattern formation, and mixing in active suspensions. *Physics of Fluids*, **20**, 123304.

Simha R. A. and Ramaswamy S. (2002). Hydrodynamic fluctuations and instabilities in ordered suspensions of self-propelled particles. *Physical Review Letters*, **89**, 58101.

Smith D. J, Gaffney E. A., Gadêlha H., Kapur N., and Kirkman-Brown J. C. (2009). Bend propagation in the flagella of migrating human sperm, and its modulation by viscosity. *Cell Motility and the Cytoskeleton*, **66**, 220–236.

Sokolov A., Aranson I. S., Kessler J. O., and Goldstein R. E. (2007). Concentration dependence of the collective dynamics of swimming bacteria. *Experiments in Fluids*, **43**, 737.

Spagnolie S. E. and Lauga E. (2010). The optimal elastic flagellum. *Physics of Fluids*, **22**, 031901.

Tam D. and Hosoi A. E. (2007). Optimal stroke patterns for Purcell's three-link swimmer. *Physical Review Letters*, **98**, 68105.

94   *Dynamics of complex biofluids*

Taylor G . I. (1951). Analysis of the swimming of microscopic organisms. *Proceedings of the Royal Society of London, Series A, Mathematical and Physical Sciences*, **209**, 447–461.

Teran J., Fauci L. J., and Shelley M. J. (2008). Peristaltic pumping and irreversibility of a Stokesian viscoelastic fluid. *Physics of Fluids*, **20**, 073101.

Teran J., Fauci L. J., and Shelley M. J. (2010). Viscoelastic fluid response can increase the speed and efficiency of a free swimmer. *Physical Review Letters*, **104**, 38101.

Thomases B. and Shelley M. J. (2007). Emergence of singular structures in Oldroyd-B fluids. *Physics of Fluids*, **19**, 103103.

Thomases B. and Shelley M. J. (2009). Transition to mixing and oscillations in a Stokesian viscoelastic flow. *Physical Review Letters*, **103**, 094501.

Tuval I., Cisneros L., Dombrowski C., Wolgemuth C. W., Kessler J. O., and Goldstein R. E. (2005). Bacterial swimming and oxygen transport near contact lines. *Proceedings of the National Academy of Sciences*, **102**, 2277.

Underhill P. T., Hernández-Ortiz J. P., and Graham M. D. (2008). Diffusion and spatial correlations in suspensions of swimming particles. *Physical Review Letters*, **100**, 248101.

Walker S. W. and Shelley M. J. (2010). Shape optimization of peristaltic pumping. *Journal of Computational Physics*, **229**, 1260–1291.

Young Y. N. and Shelley M. J. (2007). Stretch-coil transition and transport of fibers in cellular flows. *Physical Review Letters*, **99**, 58303.

Zerrouki D., Baudry J., Pine D., Chaikin P., and Bibette J. (2008). Chiral colloidal clusters. *Nature*, **455**, 380–382.